

# Simulating convection-coupled phase-change in enthalpy form with mixed finite elements

Alexander G. Zimmerman<sup>a</sup>, Julia Kowalski<sup>a</sup>

<sup>a</sup>*RWTH Aachen University, Templergraben 55, 52062 Aachen, Germany*

---

## Abstract

Melting and solidification processes are often affected by natural convection of the liquid, posing a multi-physics problem involving fluid flow, convective and diffusive heat transfer, and phase-change reactions. Enthalpy methods formulate this convection-coupled phase-change problem on a single computational domain. The arising system of governing equations can be solved accurately with a monolithic approach using mixed finite elements and Newton's method. Previously, the monolithic approach has relied on adaptive mesh refinement to regularize local nonlinearities at phase interfaces. This contribution instead separates mesh refinement from nonlinear problem regularization and provides a robust continuation procedure to obtain accurate solutions on uniform meshes. A flexible and extensible open source implementation is provided. The code is formally verified to accurately solve the governing equations and convergence rates are shown. Simulations are presented with comparison to two experimental data sets, one for the melting of octadecane and another for the freezing of water. Furthermore, the robust solution procedure admits detailed sensitivity studies with respect to key numerical parameters. For the case of freezing water, effective reduction of numerical errors from these key parameters is successfully demonstrated.

*Keywords:* Computational fluid dynamics, phase-change, mixed finite elements, nonlinear, regularization, Firedrake

---



---

*Email address:* `zimmerman@ices.rwth-aachen.de` (Alexander G. Zimmerman)

*Preprint submitted to arXiv*

*May 31, 2022*

## Nomenclature

$\mathcal{F}$	Nonlinear problem residual	$\kappa$	Thermal conductivity
$b$	Buoyancy function	$\mu$	Dynamic viscosity
$\phi$	Regularized volume fraction	$\nu$	Kinematic viscosity
$T$	Temperature	$\rho$	Density
$p$	Pressure	Gr	Grashof number
$t$	Time	Pr	Prandtl number
$\mathbf{u}$	Velocity	Ste	Stefan number
$\mathbf{w}$	System solution	$\hat{\mathbf{g}}$	Direction of gravity
$\mathbf{x}$	Position	$l$	Subscript for liquid
$x$	Horizontal position	$s$	Subscript for solid
$y$	Vertical position	$\Delta t$	Time step size
$j$	Newton iteration index	$h$	Mesh cell size
$n$	Discrete time index	$q$	Quadrature degree
$C$	Volumetric heat capacity	$\sigma$	Regularization parameter
$T_m$	Phase-change temperature	$\tau$	Velocity relaxation factor

## 1. Introduction

Melting and solidification processes in phase-change materials are relevant to many areas of engineering and scientific research. Examples include the casting of metals, storage of solar and thermal energy as latent heat, and modeling phase-change processes in the cryosphere, e.g. as relevant for climate projections. In some regimes, the phase-change process is substantially affected by convection in the liquid phase, which has been demonstrated in a number of experiments [1, 2, 3, 4, 5].

Any spatiotemporally resolved simulation of this multi-physics process is a mathematical and computational challenge. Common modeling strategies couple systems of multi-parameter nonlinear partial differential equations resulting from the balance laws of mass, momentum, and energy. For realistic

scenarios, solving the system requires efficient and robust numerical methods. The design and validation of models for different regimes and the formulation of accurate solution methods are areas of ongoing research.

The current work focuses on pure materials at macroscopic scale, for which melting and freezing occur at one specific temperature, namely the melting/freezing point  $T_m$ . The corresponding phase-change process is commonly referred to as *isothermal* phase-change [6]. Isothermal phase-change produces well defined, distinct phase interfaces at small spatial scales. There are many other materials that do not fall into this class, e.g. alloys or sea ice, and that produce substantial mushy regions. For such other materials, melting and freezing processes are bounded by solidus and liquidus temperatures which can both vary depending on the local material composition. Isothermal phase-change can hence be interpreted as the limiting case, in which the solidus and liquidus temperatures coincide and are constant.

Many computational fluid dynamics (CFD) applications are concerned with a physical setting that consists of entirely gas or entirely liquid materials, sometimes extending into multi-phase gas-liquid applications. In these cases, solids exist only as boundaries and are usually fixed in space and time. Simulating convection-coupled melting and freezing requires the extension of CFD into multi-phase liquid-solid applications. This involves modeling the spatiotemporally evolving interfaces between liquids and solids. For this, one can use either an interface tracking or an interface capturing method [6, 7]. Interface tracking methods explicitly track the phase interfaces, solve separate systems of governing equations in each phase domain, and enforce coupling constraints at the interfaces. Interface capturing methods instead solve one system of governing equations on a single domain that is occupied by both phases. Interface capturing handles phase interfaces implicitly. The phase interfaces can be post-processed as an explicit function of the solution.

The current work uses an interface capturing method that relies on an enthalpy formulation of the phase-change process. This is often also referred to as an enthalpy method [6]. Enthalpy methods write the energy balance in terms of both the temperature and the enthalpy, and hence need to be closed with an equation relating these two quantities. For incompressible materials, this relation is well-understood and can be easily phrased in terms of the liquid and solid phase volume fractions. Enthalpy methods can hence be closed by assuming an equation of state relating the phase volume fractions to the material's effective temperature. Considering isothermal phase-change, the equation of state reduces to an indicator type functional relation.

This choice results in an energy balance taking the form of a standard heat equation extended by a source term which accounts for the gain or loss of latent heat at the phase interface. Enthalpy methods have been applied extensively to convection-coupled phase-change [6, 8, 9, 7, 10, 11, 12, 13, 14, 15], but there remain many opportunities for improvement.

Enthalpy methods are often applied to regimes where the velocity vanishes in solid regions. Since interfaces between phases are not tracked explicitly, typical velocity boundary conditions, such as the commonly used no-slip condition, cannot be applied directly. Rather, different modeling techniques are used to guarantee a vanishing velocity in the solid phase. These are sometimes referred to as a *solid velocity correction* [16]. Different approaches are compared in [6, 17]. Three primary approaches to solid velocity correction have prevailed:

1. modifying the algorithm to directly set the velocity to zero in the solid regions [16],
2. adding a phase-dependent source term to the momentum equation, forcing the velocity to relax to zero in the solid region [12, 5, 15], and
3. prescribing a phase-dependent viscosity with orders of magnitude larger values in the solid than in the liquid phase [13, 14].

The first approach provides a pragmatic *brute force* solution and allows no velocity dampening close to the phase interface. The second and third approaches both rely on additional numerical parameters that can affect the evolution of phase interfaces. Critically, these new parameters, which initially do not have any physical significance, must be calibrated based on experimental data, as seen in [15] or [13]. This need for calibration may undermine the predictiveness of the models, because it is not clear to what extent the calibrated parameters also apply to other physical regimes or geometric settings. Furthermore, recent applications of the second approach to isothermal convection-coupled phase-change, e.g. [12, 5, 15], have used the Kozeny-Carman relation in the momentum source term. This contrasts with the explanation in [6, 9] that the Kozeny-Carman relation is most physically relevant for non-isothermal mushy region phase-change. A simpler formulation of the velocity relaxation can be assumed for isothermal phase-change of pure materials [9, 11] and will be leveraged in the current article.

For any chosen approach to solid velocity correction, the step change in velocity at phase interfaces disrupts nonlinear solver convergence [9]. A common regularization approach is to introduce a temperature range in which the

phase-change occurs rather than restricting it to exactly the melting/freezing point. There seems to be a strong analogy between this type of numerical method and the physical situation of non-isothermal phase-change for non-pure materials. In both situations, the community tends to refer to the lower and upper temperature bounds respectively as solidus and liquidus temperatures. It is, however, important to distinguish cases in which solidus and liquidus temperatures are physically motivated versus cases in which they are introduced only to stabilize an otherwise unstable computational model. Simulations in the current work consider sensitivity to the phase interface regularization, and reduce the regularization until it does not create unphysical mushy layers or substantially affect the shape of phase interfaces.

Enthalpy methods define a system of partial differential equations which must be discretized in space and time. Many approaches have been applied for spatial discretization, including finite differences [6, 8, 9], finite volumes [10, 11, 16, 5], the finite element method (FEM) with operator splitting [12], and monolithic mixed FEM [13, 14, 15, 18]. The formulations in [13, 14, 15, 18] all used Taylor-Hood elements simultaneously with the pressure penalty method to stabilize the mixed finite element system. Taylor-Hood elements increase the degree of the velocity basis, adding a degree of freedom per cell in each dimension. The current work demonstrates successful stabilization using the pressure penalty method alone. In the context of enthalpy formulated convection-coupled phase-change, the stability of mixed FEM schemes was analyzed for the first time in [18]. Also in this context, per the current authors' knowledge, the only formal accuracy verifications of implemented solvers are in [18] and in the current work. Both use the method of manufactured solutions to verify the orders of accuracy of the spatial and temporal discretizations. Typically, temporal discretization is performed with finite differences. Second-order accurate fully implicit finite difference temporal discretization was advocated in [11] and subsequently used in [12, 15].

Based on the approach in [13], an open source implementation was published in [14]. Both used mixed finite elements in space and the backward Euler method in time. While the results in both [13] and [14] were promising, the nonlinear solvers were not robust. Convergence required carefully chosen time step sizes, dynamic adaptive mesh refinement (AMR), and artificial initialization of the new phase in one-way melting or solidification processes. AMR requires an *a posteriori* error estimate, which in turn requires first obtaining a solution on a coarse or manually refined mesh [14]. Furthermore,

it has not been shown that the benefits of AMR outweigh the costs. The benefit of reduced degrees of freedom competes with the cost of dynamic remeshing. The phase interfaces are moving in time, and the locations of these interfaces are where the mesh must be locally refined. The possible benefit of per-element accuracy from locally refined meshes competes with interpolation errors between non-matching meshes of different time steps. At least for two-dimensional geometries, more accurate solutions might be obtained with less computational cost on static uniform meshes.

This article is structured as follows: Section 2 presents an enthalpy formulation for convection-coupled phase-change processes with a generalized approach to phase-interface regularization. Section 3 presents a monolithic solver approach with mixed finite elements, implicit time discretization, and Newton’s method. Motivated by [9, 14], a robust continuation procedure for solving the nonlinear problem is introduced. Section 4 introduces an open-source implementation and describes the open-source libraries on which it depends. The solver’s second order accuracy is verified both in space and time. Section 5 compares simulation results both for the melting of octadecane and for the freezing of water to experimental data from the literature.

## 2. Physical and mathematical model

### 2.1. *Physical regime*

The current work focuses on simulating melting and solidification processes that are strongly influenced by convection of the liquid phase. Particularly, the focus is on regimes where there is a strong two-way coupling between the fluid dynamics and the evolving shapes of phase interfaces. The liquid is assumed as an incompressible Newtonian fluid undergoing natural convection. Following a Boussinesq assumption, the fluid density is assumed to only depend on the temperature. In this case, the flow is driven by buoyancy resulting from temperature gradients. Furthermore, the focus is on pure materials such as octadecane and distilled water. Such materials undergo isothermal phase-change [6, 9]. This means that melting and solidification occur at a single temperature.

### 2.2. *Phase interface regularization*

Consider a phase-change material which can either be solid, liquid, or a mixture of the two phases. Any small reference volume of this material has a liquid volume fraction  $f_l$  and a solid volume fraction  $f_s$ . Assuming there

are no other phases, e.g. no gas inclusions,  $f_l + f_s = 1$ . When the material is fully liquid,  $f_l = 1$ . When it is fully solid,  $f_l = 0$ . In this case, the value of  $f_l$  can be used as a substitute for the phase state.

Isothermal phase-change processes are characterized by having distinct interfaces between phases. At these interfaces, the temperature of the material is at the melting/freezing point  $T = T_m$ . In liquid regions,  $T > T_m$ . In solid regions,  $T < T_m$ . This means that the liquid volume fraction  $f_l$  can be reconstituted from the temperature alone, i.e.

$$f_l = \begin{cases} 0, & T < T_m \\ 1, & T > T_m \end{cases} \quad (1)$$

With this model, phase interfaces are theoretically infinitesimally thin lines in two-dimensional space or surfaces in three-dimensional space. The phase interfaces can be regularized by convoluting  $f_l$  with a Gaussian kernel, e.g.

$$\zeta(T) = \frac{1}{\sigma\sqrt{2\pi}} \exp\left(\frac{-T^2}{2\sigma^2}\right) \quad (2)$$

yielding

$$\phi_l = (f_l * \zeta)(T) = \frac{1}{2} \left( 1 + \operatorname{erf} \left( \frac{T - T_m}{\sigma\sqrt{2}} \right) \right) \quad (3)$$

This introduces a parameter,  $\sigma$ , which is always positive. As  $\sigma$  approaches zero,  $\phi_l$  approaches  $f_l$ . Alternative regularizations of phase interfaces that rely on similar parameters have been proposed in other literature [13, 14, 15]. With too large of  $\sigma$ , substantial regions may develop where  $0 < \phi_l < 1$ . Such regions are numerical artifacts. The parameter  $\sigma$  exists solely to make solutions computable. Therefore, for results in Section 5,  $\sigma$  was reduced until regions where  $0 < \phi_l < 1$  were small and until the shapes of the  $T = T_m$  contours were not affected.

### 2.3. Governing equations

Convection-coupled phase-change can be simulated in enthalpy form [6] using the following governing equations, which are balances of mass, momentum, and energy

$$\nabla \cdot \mathbf{u} = 0 \quad (4)$$

$$\rho_0(\partial_t \mathbf{u} + \nabla \mathbf{u} \cdot \mathbf{u}) + \nabla p - 2\nabla \cdot (\mu \operatorname{sym} \nabla \mathbf{u}) + \rho \mathbf{g} + d\phi_s \mathbf{u} = 0 \quad (5)$$

$$\partial_t (C(\mathcal{T} - \mathcal{T}_0)) + \rho_l L \partial_t \phi_l + \mathbf{u} \cdot \nabla (C(\mathcal{T} - \mathcal{T}_0)) - \nabla \cdot (\kappa \nabla \mathcal{T}) = 0 \quad (6)$$

The independent unknowns are pressure  $p$ , velocity  $u$ , and temperature  $\mathcal{T}$ . The mass equation (4) is the continuity equation for an incompressible material. The momentum equation (5) begins with the incompressible Navier-Stokes momentum equation with two additional terms. The first additional term,  $\rho \mathbf{g}$ , is a Boussinesq buoyancy term with temperature-dependent  $\rho = \rho(\mathcal{T})$ . Under the Boussinesq approximation, density variations are only considered with respect to the temperature. The incompressible flow considers a reference density  $\rho_0$ . The symmetric part of the rate-of-strain tensor is  $\text{sym} \nabla u$ .

The second additional term to the momentum equation,  $d\phi_s u$ , with  $d \gg 1$ , forces the velocity toward zero in the solid region. This is sometimes referred to as the solid velocity correction [16]. The regularized solid volume fraction is  $\phi_s$ , with  $\phi_l + \phi_s = 1$ . This solid velocity correction term is similar to that proposed in [9] for isothermal phase-change. In other recent work applied to isothermal phase-change [12, 13, 5, 15], the Kozeny-Carman relation  $d\phi_s^2 (\phi_l^3 + \epsilon)^{-1}$  was instead used. In addition to being a nonlinear function of  $\phi_s$ , the Kozeny-Carman relation adds a new parameter  $\epsilon$  which is needed to avoid division by zero. The Kozeny-Carman relation was designed to account for the effects of permeability in porous media. For this reason, it is sometimes used in enthalpy methods applied to non-isothermal phase-change processes that involve substantial mushy layers. Given no physical justification for applying the Kozeny-Carman relation to isothermal phase-change, the simpler term  $d\phi_s u$  is instead used in the current work. The same choice was made in [11], where a pure material was also simulated.

The energy balance is in enthalpy form [6]. This invokes a reference temperature  $\mathcal{T}_0$  and produces a source term accounting for the phase-change with latent heat  $L$ . The volumetric heat capacity  $\mathcal{C}$  and thermal conductivity  $\kappa$  can both depend on the phase. The volume-averaged values are  $\mathcal{C} = \phi_l \rho_l c_l + \phi_s \rho_s c_s$  and  $\kappa = \phi_l \kappa_l + \phi_s \kappa_s$ .

#### 2.4. Nondimensionalization

Based on the approach in [13], the independent variables were nondimensionalized with respect to characteristic scales. These include spatial scale  $X$ , speed scale  $U = \nu_l/X$ , and temperature scale  $T$ . The liquid material properties were used as reference values, e.g. the liquid kinematic viscosity  $\nu_l$ . Additionally, the reference temperature was chosen as the isothermal melting and freezing temperature, i.e.  $\mathcal{T}_0 = \mathcal{T}_m$ . The nondimensional variables



were chosen to be

$$\mathbf{x} = \frac{\chi}{X}, \quad t = \frac{tU}{X}, \quad p = \frac{p}{\rho_l U^2}, \quad \mathbf{u} = \frac{\mathbf{u}}{U}, \quad T = \frac{\mathcal{T} - \mathcal{T}_m}{T}, \quad (7)$$

In this case, the nondimensional melting and freezing temperature is always  $T_m = 0$ . The phase-dependent material properties were normalized with respect to the liquid values, i.e.

$$\kappa = \frac{1}{\kappa_l} (\kappa_s \phi_s + \kappa_l \phi_l) = \frac{\kappa_s}{\kappa_l} + \left(1 - \frac{\kappa_s}{\kappa_l}\right) \phi_l, \quad (8)$$

$$C = \frac{1}{\rho_l c_l} (\rho_s c_s \phi_s + \rho_l c_l \phi_l) = \frac{\rho_s c_s}{\rho_l c_l} + \left(1 - \frac{\rho_s c_s}{\rho_l c_l}\right) \phi_l \quad (9)$$

In nondimensional form, the governing equations (4), (5), and (6) then read

$$\nabla \cdot \mathbf{u} = 0, \quad (10)$$

$$\partial_t \mathbf{u} + \nabla \mathbf{u} \cdot \mathbf{u} + \nabla p - 2\nabla \cdot \text{sym} \nabla \mathbf{u} + \text{Gr } b \hat{\mathbf{g}} + \frac{1}{\tau} \phi_s \mathbf{u} = 0, \quad (11)$$

$$\partial_t (CT) + \frac{1}{\text{Ste}} \partial_t \phi_l + \mathbf{u} \cdot \nabla (CT) - \frac{1}{\text{Pr}} \nabla \cdot (\kappa \nabla T) = 0 \quad (12)$$

where the Grashof, Stefan, and Prandtl numbers are defined as

$$\text{Gr} = \frac{gL^3\beta_0 T}{\nu_l^2}, \quad \text{Ste} = \frac{c_l T}{L}, \quad \text{Pr} = \frac{\nu_l}{\alpha_l}, \quad (13)$$

In the solid velocity correction term,  $\tau$  is the nondimensional velocity relaxation factor. In the Boussinesq buoyancy term,  $b$  represents a general temperature-dependent density model which must be specified for a given liquid. In cases where this density model is nonlinear, e.g. when accounting for the density anomaly observed in water, a constant reference value  $\beta_0$  must be chosen for the thermal expansion coefficient. The liquid thermal diffusivity is  $\alpha_l = k_l/(\rho_l c_l)$ .

When referring to the governing equations in the remainder of this article, only the nondimensional system (10, 11, 12) is considered. The scaling highlights the regimes of natural convection and phase-change. For example, Section 5 presents simulations of laboratory scale experiments for the melting of octadecane and freezing of water, and describes the cases in terms of their similarity parameters. The code presented in Section 4 solves the nondimensional equations.

### 3. Numerical methods

The time-dependent problem was solved as a sequence of initial boundary values problems. Mixed finite elements were used for the spatial discretization. Backward difference formulas were used for the temporal discretization. For the current work, non-homogeneous Dirichlet and homogeneous Neumann boundary conditions were applied to the temperature field, homogeneous Dirichlet boundary conditions were applied to the velocity field. The nonlinear system was solved with Newton's method. Robustly and accurately solving the nonlinear problem required special attention to its regularization, for which a continuation procedure was developed.

#### 3.1. Spatial discretization

Following a similar approach to [13, 14], mixed finite elements were used to approximate the system (10, 11, 12) with basis functions  $\psi_p, \boldsymbol{\psi}_u, \psi_T$ , yielding the weak form residual

$$\begin{aligned} \mathcal{F} = & (\psi_p, \nabla \cdot \mathbf{u} + \gamma p) + \left( \boldsymbol{\psi}_u, \partial_t \mathbf{u} + \nabla \mathbf{u} \cdot \mathbf{u} + \text{Gr } b \hat{\mathbf{g}} + \frac{1}{\tau} \phi_s \mathbf{u} \right) \\ & - (\nabla \cdot \boldsymbol{\psi}_u, p) + 2 (\text{sym} \nabla \boldsymbol{\psi}_u, \text{sym} \nabla \mathbf{u}) \\ & + \left( \psi_T, \partial_t (CT) + \frac{1}{\text{Ste}} \partial_t \phi_l + \mathbf{u} \cdot \nabla (CT) \right) + \frac{1}{\text{Pr}} (\nabla \psi_T, \kappa \nabla T) \end{aligned} \quad (14)$$

where  $(u, v) = \int u v d\mathbf{x}$  and  $(\mathbf{u}, \mathbf{v}) = \int \mathbf{u} \cdot \mathbf{v} d\mathbf{x}$ .

Piece-wise linear polynomials were used for all basis functions. Since these do not satisfy the LBB compatibility condition for the incompressible Navier-Stokes system [19], the system was stabilized via the pressure penalty method with  $\gamma = 10^{-7}$ . This also ensures the uniqueness of the pressure solution [18]. For similar problems, a combination of both the pressure penalty method and Taylor-Hood elements had been used in [13, 14, 18]. This means that, where a piece-wise linear basis approximates the velocity field in the current work, [13, 14] used piece-wise quadratic approximations without improving the order of accuracy. With  $N$  cells of a mesh in  $D$ -dimensional space, the equal-order basis has  $ND^2$  less degrees of freedom than the Taylor-Hood basis. In Section 4, this spatial discretization's second order accuracy is verified.

$k$	$a_0$	$a_1$	$a_2$	$a_3$
1	1	-1		
2	3/2	-2	1/2	
3	11/6	-3	3/2	-1/3

Table 1: Coefficients for backward difference formulas up to third order, taken from [20]. For example, the backward Euler method is given by  $k = 1$ , and BDF2 is given by  $k = 2$ .

### 3.2. Temporal discretization

The time derivatives were discretized with the family of  $k^{\text{th}}$  order constant time step size ( $\Delta t$ ) backward difference formulas (BDF- $k$ ) [20]. For some unknown  $w^n$  at time step  $n$ , these can be written as

$$\partial_t w = \frac{1}{\Delta t} \sum_{i=0}^k a_i w^{n-i} \quad (15)$$

where the coefficients  $a_i$ , shown in Table 1 depend only on  $k$ . This requires storing solutions from the previous  $k$  time steps. For example,  $w^{n-1}$  refers to the already computed solution from the previous time step.

In addition to the independent unknowns, (15) was applied directly to  $\phi_l$  and to  $CT$  in (12). For example, applying the second order formula (BDF2) to the liquid volume fraction yields  $\partial_t \phi_l = (3\phi_l(T^n) - 4\phi_l(T^{n-1}) + \phi_l(T^{n-2})) / (2\Delta t)$ . BDF2 was used for the solver verification in Section 4 and for the simulations in Section 5.

### 3.3. Nonlinear solution with continuation

Many terms in the residual (14) are highly nonlinear. The nonlinear system was solved with Newton's method as follows. Consider the vector-valued system solution  $\mathbf{w}^n = (p^n \quad \mathbf{u}^n \quad T^n)^T$  for any discrete time step  $n$ . The nonlinear problem's solution is approximated for the next time step by solving a sequence of linear problems

$$D_{\mathbf{w}} \mathcal{F}(\mathbf{w}_j)(\mathbf{w}_{j+1} - \mathbf{w}_j) = \mathcal{F}(\mathbf{w}_j), \quad (16)$$

whose iterates  $\mathbf{w}_{j+1}$  converge to  $\mathbf{w}^n$ . Here,  $D_{\mathbf{w}} \mathcal{F}$  stands for the Gateaux derivative. It can be derived analytically, which was done for a similar problem in [14]. Or as done in the current work, it can be automatically computed with the symbolic capabilities of the software in Section 4. Each iteration of (16) is a linear system which can be solved robustly with a direct solver.

When trying to solve the nonlinear problem for the solution  $\mathbf{w}^n$  at time step  $n$ , it was first attempted to use the known solution  $\mathbf{w}^{n-1}$  from the previous time step as an initial guess. With small regularization parameter  $\sigma$  in (3), it turned out that  $\mathbf{w}^{n-1}$  was not a suitable initial guess. In [13, 14], this issue was resolved via adaptive mesh refinement, careful selection of the time step size, and suitably tailored initialization of a melt layer in melting problems or a frozen layer in freezing problems. In the current work, the nonlinear problem was solved robustly with a continuation procedure. Initial guesses were improved by solving intermediate problems with an increased value of the regularization parameter  $\sigma$ . Whenever a solution was found, it was used as an initial guess for solving the same system again, albeit with a smaller value of  $\sigma$ . The challenge hence is to find a sequence of  $\sigma$  values resulting in converging intermediate steps that reach the originally specified value. Figure 1 explains the procedure in more detail.

The resulting sequence of intermediate regularizations depends on the exact nonlinear solver method used, and on its options such as convergence criteria and maximum iterations. It was found that using the relative residual as a convergence criteria would allow for significant accumulation of error in the absolute residual between time steps. For this reason, the relative tolerance convergence criteria was disabled. The nonlinear solver was limited to twenty-four maximum iterations to reach the convergence criteria. Section 5 reports the total number of Newton iterations for each of the selected simulations. Despite having to solve a sequence of nonlinear problems for each time step, the total numbers of Newton iterations were not excessively high, because the successfully solved intermediate problems converge optimally.

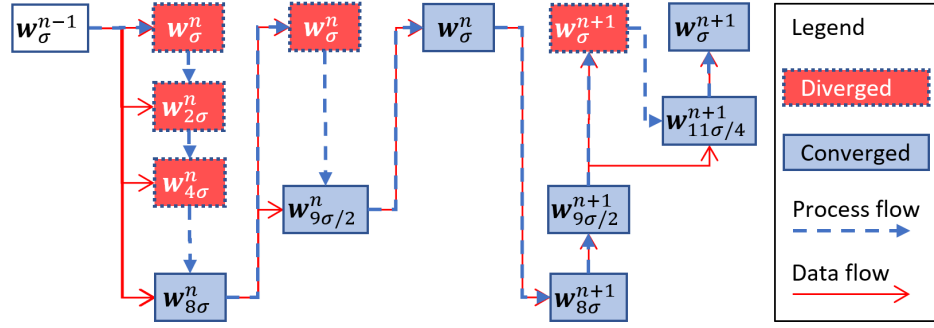


Figure 1: Continuation procedure for robustly solving the nonlinear problem. Consider the nonlinear problem  $\mathcal{F}_\sigma(\mathbf{w}^n) = 0$  with regularization parameter  $\sigma$  at time step  $n$ . Its solution is denoted by  $\mathbf{w}_\sigma^n$ . When applying Newton's method to find  $\mathbf{w}_\sigma^n$ , it was first attempted to use the known solution from the previous time step, i.e.  $\mathbf{w}_\sigma^{n-1}$ , as the initial guess. For this, the solver would diverge. Better initial guesses were obtained by solving the problem with larger intermediate values for  $\sigma$ . In particular, the value can be recursively doubled until a solution is found, which terminated at  $8\sigma$  in this figure. The intermediate solution is denoted by  $\mathbf{w}_{8\sigma}^n$ . Then,  $\mathbf{w}_{8\sigma}^n$  was used as the initial guess for solving the original problem. When  $\mathbf{w}_{8\sigma}^n$  was still not an adequate initial guess, the next attempted  $\sigma$  value was taken as the average of the target value  $\sigma$  and the nearest successful value  $8\sigma$ , i.e.  $9\sigma/2$ . The procedure was repeated until successfully finding  $\mathbf{w}_\sigma^n$ . Successful sequences of intermediate  $\sigma$  values were used for subsequent time steps, as shown in this figure to reach  $\mathbf{w}_\sigma^{n+1}$ . Again, when the solver failed, a new intermediate value was inserted.

## 4. Implementation and verification with open-source libraries

In order to reduce the required coding effort, leverage state-of-the-art methods and solvers, and increase the usability of the software and reproducibility of results, the code was implemented using the open source finite element library Firedrake [21]. On top of Firedrake, for this work, the open source Sapphire [22] framework was developed. Its purpose is to construct time dependent simulations using the methods from Section 3. The convection-coupled phase-change simulations used to obtain the results in Section 5 were implemented within the Sapphire framework.

### 4.1. *Firedrake*

In recent years, a technology has been developed to automatically implement finite element discretizations of variational problems, the Unified Form Language (UFL) [23]. UFL provides a domain specific language for users to abstractly define their problem, and automatically writes and compiles efficient C++ code. From the existing libraries based on UFL, this work used Firedrake [21]. In addition to finite element discretization, Firedrake was used to generate meshes of simple geometries, to interface with efficient linear and nonlinear solvers from PETSc [24], and to output solutions to a standard format. Firedrake is designed for performance portability [25, 26]. For the results presented in Section 5, all linear systems were solved with MUMPS [27, 28], and all nonlinear systems were solved with PETSc’s SNES (Scalable Nonlinear Equations Solvers) line search method, both via the Firedrake interfaces.

By default, Firedrake automatically determines the quadrature degree for a given problem. Alternatively, the user can specify a degree. In the current work, when integrating the regularized liquid volume fraction (3) with small regularization parameter value  $\sigma$ , Firedrake automatically determined excessively large quadrature degrees. Computations were performed more efficiently by reducing the quadrature degree, which reduced the number of function evaluations needed for each degree of freedom when performing finite element assembly. This essentially introduced a new numerical parameter to the model, the quadrature degree,  $q$ . Therefore,  $q$  is included in the sensitivity studies of Section 5.

Firedrake depends on a stack of open source scientific software libraries. A benefit is that ongoing technological developments from a variety of open

source scientific software projects are leveraged. A downside is that the software can be difficult to configure and compile. To manage this complexity, the Firedrake project maintains an installation script. Furthermore, to facilitate the reproduction of scientific results, Firedrake provides a command line tool which installs a specified set of versions and configurations throughout the software stack. The exact versions of Firedrake and its software stack used for the results in the current work were documented with a DOI on Zenodo [29], ensuring reproducibility.

#### 4.2. *Sapphire*

Sapphire was developed for the purposes of the current work. Sapphire provides a Python class for time dependent simulations that are governed by PDE's. The PDE's must be discretized in space with finite elements and in time with finite differences. Spatial discretization is handled by Firedrake, with the PDE being defined in variational form using UFL. The time discretization module includes backward different formulas up to sixth order. Five arguments are required to instantiate a Sapphire simulation:

- a mesh, e.g. from Firedrake's built-in mesh functions or converted from an external meshing library,
- a finite element or mixed finite element defined by UFL,
- the residual of the governing equations in variational form, e.g. (14), defined by UFL,
- a (possibly empty) list of Firedrake Dirichlet boundary conditions,
- initial values as a Firedrake finite element function.

With these defined, a simulation is ready to run.

In Section 4.3, the convection-coupled phase-change solver's accuracy is verified using the method of manufactured solutions (MMS) according to the general guidelines in [30]. Manually deriving MMS source terms creates many opportunities for errors, especially for systems of PDE's involving vector calculus. Often symbolic math libraries are used to derive the source terms. Python has such a symbolic math library which does not depend on UFL. With Sapphire already depending on UFL, it was more convenient to use UFL itself for symbolically deriving the MMS source terms. An additional module in Sapphire hence uses UFL to automatically derive the source terms. The module also automatically augments the variational problem which needs to

be solved for verification. As part of its test suite, Sapphire uses the MMS module to verify the accuracy of solutions to many different PDE's.

Sapphire is a flexible tool, is publicly available, and is freely licensed. Simulations have been implemented in Sapphire which solve the heat equation, convection-diffusion, steady and unsteady incompressible Navier-Stokes, natural convection, and phase-change in enthalpy form without convection. This provided a strong base for implementing convection-coupled phase-change in enthalpy form. For the convection-coupled phase-change simulation, the most significant additional work was to implement the continuation procedure from Figure 1. The version of Sapphire used to produce the results in the current work is documented with a DOI on Zenodo [22].

#### *4.3. Solver verification*

Numerical solutions to the weak residual (14) approximate solutions to the governing equations (10, 11, 12). As there is no sufficiently complex analytical reference solution available, spatial and temporal convergence were verified via the method of manufactured solutions (MMS). MMS is a general method for verifying PDE solvers. There is an additional benefit to MMS when approximating solutions to strong form governing equations via weak formulations. In addition to verifying the code, the weak formulation is also verified, because the weak form is tested against the strong form.

A manufactured solution can be any function which is sufficiently differentiable in space and time to exercise the spatial and temporal derivatives in the governing equations. Substituting a manufactured solution, which is not an exact solution, into the governing equations yields a source term in each equation. Adding the source terms to the governing equations creates an augmented problem. To verify a solver, it is applied to the augmented problem, and the resulting solution must approximate the manufactured solution with the expected orders of accuracy. Manufactured solutions do not necessarily need to have physical interpretations [30]. The purpose is to reveal coding errors and to verify the solver.

To apply the MMS procedure for verifying a solver's spatial or temporal orders of accuracy, Sapphire requires the user to

- implement the strong form governing equations (10, 11, 12) with UFL,
- implement a manufacture solution with UFL,



- and set a single time step size  $\Delta t$  and a list of meshes with decreasing cell sizes  $h$  for spatial verification, or a single mesh and a list of  $\Delta t$  for temporal verification.

Separate manufactured solutions can be used to independently verify the spatial and temporal discretizations.

The strong form governing equations and manufactured solutions are defined in a Python module, and the verification process is run with a Python script. Then, the module is passed to one of Sapphire’s MMS verification functions. Sapphire automatically

- derives the source term for each component of the manufactured solution, multiplies them with appropriate test functions, and adds them to the weak form,
- sets initial values and boundary conditions as given by the solution,
- runs simulations for specified lists of  $h$  or  $\Delta t$ ,
- tabulates errors between the approximate finite element solutions and the manufactured solutions,
- reports convergence rates with respect to  $h$  or  $\Delta t$ ,
- and asserts that the reported convergence rate matches the expected order of accuracy within a specified tolerance.

Verification of the current convection-coupled phase-change solver was performed on a unit square domain with Dirichlet boundary conditions. The manufactured solution was

$$\begin{aligned}\mathbf{u}_M &= \exp(t/2) \sin(2\pi x) \sin(\pi y) \hat{\mathbf{i}} + \exp(t/2) \sin(\pi x) \sin(2\pi y) \hat{\mathbf{j}} \\ p_M &= -\sin(\pi x) \sin(2\pi y) \\ T_M &= 0.5 \sin(2\pi x) \sin(\pi y) (1 - \exp(-t^2/2))\end{aligned}$$

where  $x$  and  $y$  are the components of the position  $\mathbf{x}$ .

For the buoyancy term in (11), a classical linear Boussinesq model was used by setting  $b = T$ . The similarity parameters were set to  $Gr = 3.6 \times 10^5$ ,  $Pr = 7.0$ , and  $Ste = 0.13$ . The material property parameters were set to  $\rho_s/\rho_l = 0.92$ ,  $c_s/c_l = 0.50$ , and  $\kappa_s/\kappa_l = 3.8$ . The regularization parameter was set to  $\sigma = 0.1$  and the solid velocity relaxation parameter was set to  $\tau = 10^{-12}$ . The quadrature degree  $q$  was automatically set by Firedrake.

To verify spatial discretization accuracy independently of any time discretization error, the manufactured solution was evaluated at time  $t = 1$ , and no further time dependency as assumed. The resulting problem was solved in a single pseudo-time step. This was repeated on a series of uniformly refined meshes, corresponding to the mesh shown in Figure 3 with a different cell edge length,  $h$ , for each mesh. To independently verify the temporal discretization accuracy, a sufficiently refined mesh was used such that the spatial discretization error would not dominate the total error. The unsteady problem was solved repeatedly with a sequence of time step sizes  $\Delta t$ . Figure 2 shows the observed convergence orders with respect to  $h$  and  $\Delta t$ . Having applied second order accurate discretization methods, the effective orders of accuracy appear to be asymptotically approaching the theoretical values. The entire Sapphire-based verification procedure takes approximately a minute to run on a single CPU. It is included into a continuous integration process that runs automatically whenever the code’s master version on GitHub [22] is modified.

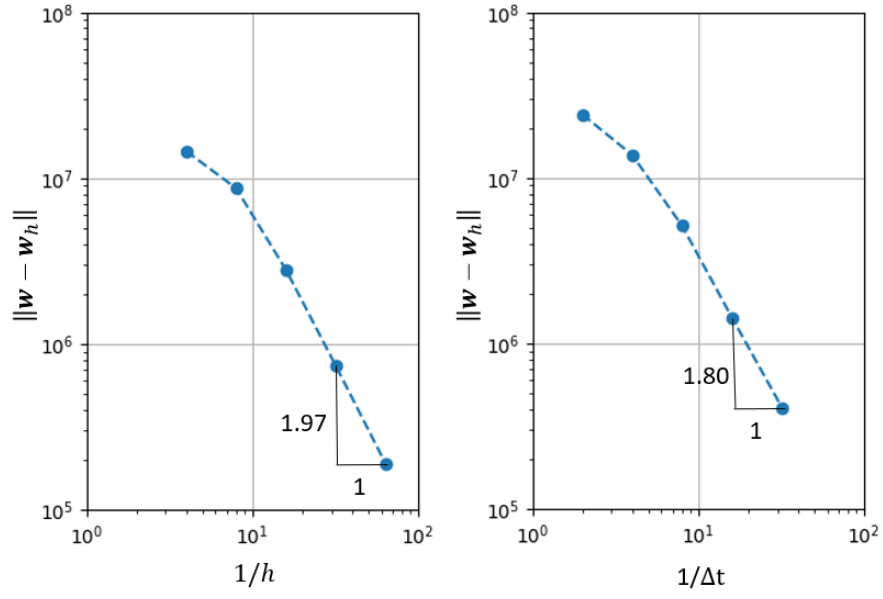


Figure 2: Verification of solver accuracy via the method of manufactured solutions. Left) The  $L^2$  norm error reduced quadratically as the time step size  $\Delta t$  was reduced. Right) The  $L^2$  norm error reduced quadratically as mesh cell edge length  $h$  was reduced. Convergence approached the expected second order accuracy both in space and time. This verified that the governing equations (10, 11, 12) were approximated accurately by the solver. Further reducing  $h$  and  $\Delta t$  should make the result more precise. In either case, the competing discretization error respectively of either  $\Delta t$  or  $h$  must also be controlled. Increasing the precision of this verification can quickly become impractical.

## 5. Validation with benchmark experiments

Two experimental data sets from the literature were considered in order to validate the implemented model. First, octadecane melting was simulated for comparison to an experiment from [3]. Second, water freezing was simulated for comparison to experiments from [4]. Both simulations were performed on unit square geometric domains, and both used the same configuration of boundary conditions shown in Figure 3, on the left. The top and bottom boundaries were assumed to be adiabatic, while the left and right walls were kept respectively at constant hot temperature  $T_h$  and cold temperature  $T_c$ . No slip velocity boundary conditions were applied on each wall. For both benchmarks, gravity points vertically downward, i.e.  $\hat{\mathbf{g}} = (0, -1)^T$ . Also in both cases, a uniform triangular mesh with cell edge length  $h$  was used. An exemplary mesh with  $h = 0.2$  is shown in Figure 3, on the right.

Each of the two following subsections is devoted to validation against one of the experiments. In both cases, the subsection includes

1. a description of the experimental setup.
2. a description of the simulation setup. This includes the scaling and similarity parameters, the phase-dependent material properties, the buoyancy model, the procedure for obtaining initial values, and the boundary condition values,
3. a sensitivity study involving five numerical parameters. These are the mesh cell size  $h$ , the time step size  $\Delta t$ , the phase interface regularization parameter  $\sigma$ , the solid velocity relaxation parameter  $\tau$ , and the quadrature degree  $q$ . With respect to a nominal set of parameters values, each parameter is varied individually and the resulting phase interfaces are evaluated at a fixed time.
4. a selected simulation result. The selection is based on the sensitivity study. The numerical parameters for the selected case are reported. The temperature field and velocity streamlines are visualized at multiple time steps. The simulated phase interface is compared to the experiment at multiple times.

### 5.1. Melting octadecane

The melting of octadecane was simulated for comparison to an experiment from [3]. In the experiment, a slab of octadecane was insulated on the top and bottom. The material was initially at its melting temperature. One side was heated to melt the material.

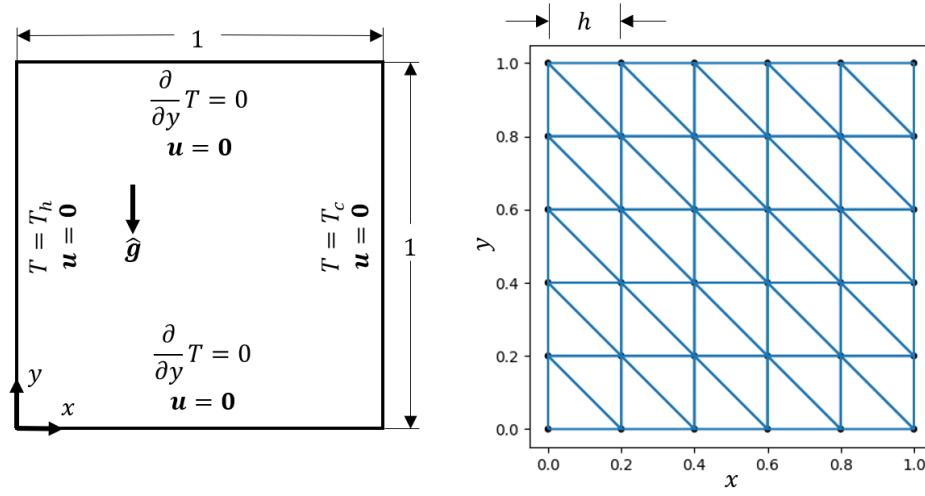


Figure 3: The geometric domain, boundary conditions, and mesh.

Left) For all computations, the geometric domain was the unit square. The left wall was kept constant at a higher temperature,  $T_h$ . The right wall was kept constant at a lower temperature,  $T_c$ . The top and bottom walls were adiabatic. All walls had no slip conditions on the velocity. The direction of gravity for the momentum equation (11) was  $\hat{\mathbf{g}} = (0, -1)^T$ . Right) A uniform triangular mesh of the unit square domain. The cell edge length is  $h$ . Here,  $h = 0.2$ . The sensitivity studies in this section include  $0.005 \leq h \leq 0.04$ .

### 5.1.1. Simulation set-up

The height of the experimental cavity as taken from [3] was used as the length scale, i.e.  $X = 0.015$  m. A realistic value for the liquid kinematic viscosity,  $\nu_l = 10^{-5}$  m<sup>2</sup>/s as taken from [16], furthermore yields the characteristic time scale  $X^2/\nu_l = 22.5$  s. Based on physical parameters provided in [13] and according to the previously introduced definitions (13), the similarity parameters are  $Gr = 5820$ ,  $Pr = 56.2$ , and  $Ste = 0.0450$ . Octadecane has approximately constant volumetric heat capacity and thermal conductivity between phases. Therefore the normalized values for the energy balance (12) are  $C = \kappa = 1$ . Finally, a linear Boussinesq model with constant thermal expansion coefficient is assumed. Given the defined Grashof number (13), this yields  $b = T$  for the momentum balance (11).

For the nondimensional temperature corresponding to the melting point, i.e.  $T = T_m = 0$ , the regularized liquid volume fraction as defined in (3) is evaluated to be  $\phi_l = 0.5$ . This is true for any chosen regularization parameter  $\sigma$ . In order to capture the experimental conditions, in which the material at time zero had been solid with a temperature close to the melting temperature, the initial temperature for the simulation was offset by a small amount, i.e.  $T_0 = -0.01$ . This approach follows earlier work, e.g. [13, 14, 15]. For this particular choice of the initial temperature  $T_0$ , setting  $\sigma = 0.004$  yields an initial liquid volume fraction  $\phi_l = 0.006$ , meaning that more than 99% of the material is initially solid.

During the experiment, the left boundary was kept at a constant temperature well above the melting point, while the right boundary was kept at a temperature close to the melting point. For the simulation boundary conditions shown in Figure 3, this translates into  $T_h = 1$  and  $T_c = T_0$ . The high temperature at the left boundary causes melting from left to right.

### 5.1.2. Sensitivity to numerical parameters

For this sensitivity study, the nominal parameter values were  $h = 0.01$ ,  $\Delta t = 1$ ,  $\sigma = 0.004$ ,  $\tau = 10^{-12}$ , and  $q = 4$ . From their nominal values, each parameter was varied independently. The resulting phase interfaces were compared at time  $t = 79$ . The results are shown in Figure 4. The time  $t = 79$  is also the final simulated time presented in Figure 5.

The mesh cell size,  $h$ , was varied from a maximum of  $h = 0.04$  to a minimum of  $h = 0.005$ . The upper part of the phase interface was most sensitive to  $h$ . Between the smallest values,  $h = 0.01$  and  $h = 0.005$ , the position of the phase interface in the upper portion of the domain still visibly changed;

but overall there appeared to be an asymptotic convergence behavior. The time step size,  $\Delta t$ , was varied from a maximum of  $\Delta t = 1.975$  to a minimum of  $\Delta t = 0.25$ . For the largest size,  $\Delta t = 1.975$ , there was a significant decrease in the melting near the top wall. For  $\Delta t \leq 1$ , the result was no longer significantly changed by reducing  $\Delta t$ .

The regularization parameter,  $\sigma$ , was varied from a maximum of  $\sigma = 0.008$  to a minimum of  $\sigma = 0.001$ . For the largest value,  $\sigma = 0.008$ , the entire phase interface shifted rightward. This was because, at the initial temperature  $T_0 = -0.01$ , the initial liquid volume fraction was  $\phi_l = 0.1056$ . This meant that about ten percent of the material was already melted at the initial time, shifting the entire phase interface in the direction of melting. For  $\sigma = 0.004$ , less than one percent of the material was melted at the initial time, and this effect no longer appeared to dominate. Between the three smaller values of  $\sigma$  ranging from  $\sigma = 0.004$  to  $\sigma = 0.001$ , there appeared to be little sensitivity.

The solid velocity relaxation parameter,  $\tau$ , was varied from a maximum of  $\tau = 10^{-8}$  to a minimum of  $\tau = 10^{-14}$ . For the largest value,  $\tau = 10^{-8}$ , significantly more melting occurred near the top wall. Between the three smallest values of  $\tau$  ranging from  $\tau = 10^{-10}$  to  $\tau = 10^{-14}$ , there appeared to be little sensitivity. The quadrature degree,  $q$ , was varied from a minimum of 2 to a maximum of 16. For the smallest value,  $q = 2$ , significantly more melting occurred near the top wall. Between the three largest values of  $q$  ranging from  $q = 4$  to  $q = 16$ , there appeared to be little sensitivity.

### 5.1.3. Results and discussion

Figure 5 shows the temperature field, streamlines of the velocity field, and the post-processed position of the phase interface at times  $t = 40$  and  $t = 79$ . Convection in the liquid phase caused a sharper temperature gradient near the top of the phase interface than towards its bottom. This in turn caused a faster melting rate in the upper region. This effect was more pronounced at the later time.

At the final time, after a total of seventy-nine time steps, 6971 Newton iterations were used in total. This averages to about ninety Newton iterations per time step. This includes all iterations from intermediate problems during the continuation procedure sketched in Figure 1. For all time steps, the largest intermediate regularization parameter value was  $\sigma = 0.512$ . For the first time step, eight additional values ( $\sigma = 0.257, 0.1295, 0.06575, 0.033875, 0.0179375, 0.013953125, 0.0119609375, 0.00996875$ ) were needed between  $\sigma =$

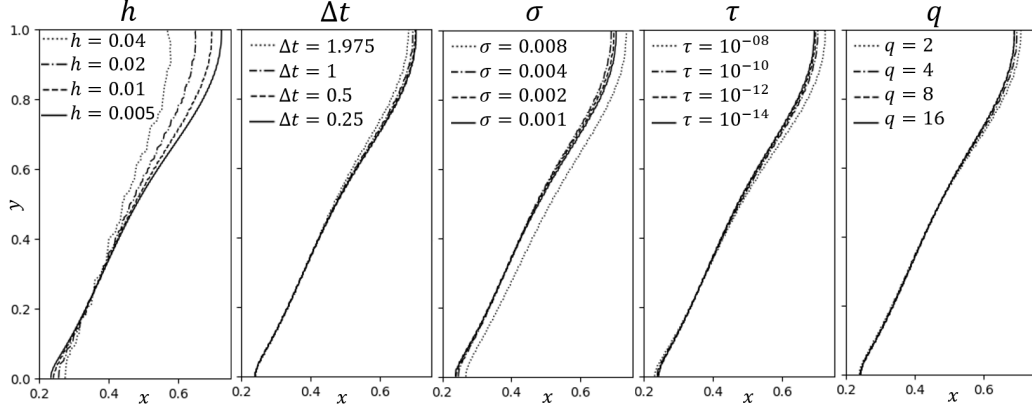


Figure 4: Sensitivity study for the octadecane melting simulation.

Five numerical parameters were varied. These were the mesh cell size  $h$ , the time step size  $\Delta t$ , the phase interface regularization parameter  $\sigma$ , the solid velocity relaxation parameter  $\tau$ , and the quadrature degree  $q$ . With respect to nominal values, each parameter was varied individually and the resulting phase interfaces were evaluated at time  $t = 79$ . The nominal values were  $h = 0.01$ ,  $\Delta t = 1$ ,  $\sigma = 0.004$ ,  $\tau = 10^{-12}$  and  $q = 4$ . Asymptotic limits are apparent for all five parameters. Between the smallest two values of  $h$ , i.e.  $h = 0.01$  and  $h = 0.005$ , the phase interface significantly changes near the top wall. Insensitivity is successfully demonstrated for small  $\Delta t$ ,  $\sigma$ , and  $\tau$ , and for large  $q$ .

0.512 and the targeted value,  $\sigma = 0.002$ . At the final time, an additional four values of ( $\sigma = 0.097625, 0.0816875, 0.07371875, 0.005984375$ ) were needed.

About half-way through the run time, at  $t = 40$ , the simulated and experimental interface positions showed good agreement both near the top and near the bottom walls. There were minor deviations in the interior. At the final time, there was good agreement for a large portion of the phase interface, but it proceeded more quickly in the experiment than in the simulation near the top and bottom walls. The previously conducted sensitivity study, shown in Figure 4, suggests that the phase interface near the top wall could agree better with the experimental data by reducing the mesh cell size  $h$ , but no such improvement should be expected near the bottom wall. It has already been reported in [15] that there is some uncertainty about the insulation of the top and bottom walls in the experiment. The phase interface as observed in the experiment is clearly not orthogonal to the top wall. A further analysis of the impact of various formulations for the boundary conditions, however, is outside of the scope of the current work. On the interior of the domain, the results compare well to the experiment. One possible way forward could



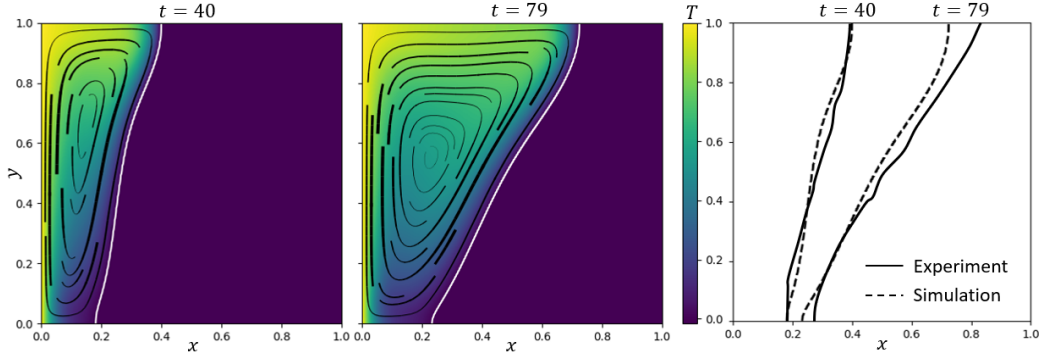


Figure 5: Octadecane melting simulation results compared to an experiment from [3]. In the experiment, a slab of octadecane was insulated on the top and bottom. The material was initially at its melting temperature. The left wall was raised to a constant temperature above the melting point in order to melt the material. The simulation used initial values and boundary conditions to match this setup. The similarity parameters were  $Gr = 5820$ ,  $Pr = 56.2$ , and  $Ste = 0.0450$ . The numerical parameters were  $h = 0.005$ ,  $\Delta t = 1$ ,  $\sigma = 0.002$ ,  $\tau = 10^{-12}$ , and  $q = 4$ . Left) Results from the simulation at time  $t = 40$ , with a colored temperature field and black velocity streamlines. The streamline thicknesses are linearly proportional to the local velocity magnitude. The white line is an isoline where  $T = 0$ , indicating the phase interface. Convection in the liquid phase caused a sharper temperature gradient near the top of the phase interface than towards its bottom. This in turn caused a faster melting rate in the upper region. Center) The same at  $t = 79$ . The effect of convection in the liquid phase on melting near the top and bottom walls is even more pronounced. Right) A comparison of the phase interfaces between the experiment and simulation at both times.

be to apply a heat flux boundary condition on the top wall instead of the adiabatic boundary condition which was used. For further validation, the experimental conditions should be examined in more detail, especially with regards to the boundary conditions.

## 5.2. Freezing water

The freezing of distilled water was simulated for comparison to benchmarking experiments in [4], where a cube of liquid water was frozen from one side. For water-ice, the density, heat capacity, and thermal conductivity vary significantly between phases. Furthermore, liquid water’s thermal expansion coefficient is nonlinear, with the sign inverting at the temperature of water’s density anomaly.

### 5.2.1. Simulation set-up

The edge length of the experimental cube’s test section, taken from [4], was used as the length scale, i.e.  $X = 0.038$  m. A realistic value for the liquid kinematic viscosity,  $\nu_l = 1.0032 \times 10^{-6}$  m<sup>2</sup>/s as taken from [31], furthermore yields the characteristic time scale  $X^2/\nu_l = 1440$ s. Based on physical parameters provided in [13] and according to the previously introduced definitions (13), the similarity parameters are  $Gr = 3.60 \times 10^5$ ,  $Pr = 6.99$ , and  $Ste = 0.125$ . Phase-dependent thermal conductivity and volumetric heat capacity were included with  $\kappa_s/\kappa_l = 3.767$  and  $(\rho_s c_s)/(\rho_l c_l) = 0.4867$  in (8) and (9). The nonlinear water density model from [13] was used. First proposed in [32], the key feature is the density anomaly of water. For example, the density anomaly caused the double convection pattern shown in Figure 6. The density is expanded around its maximum 999.972 kg/m<sup>-3</sup> which occurs at 4.0293 °C.

The simulation initial values correspond to the “warm start” initial conditions from [4]. For this, the left and right walls were respectively kept constant at hot and cold temperatures  $\mathcal{T}_h = 10$  °C and  $\mathcal{T}_c = 0$  °C. A steady state convection was reached. For the simulation, this initial temperature range was used for the temperature scale, i.e.  $T = \mathcal{T}_h - \mathcal{T}_c = 10$  °C. With this scale, the dimensionless boundary temperatures were  $T_h = 1$  and  $T_c = 0$ . The steady state problem was solved directly. Therefore, the liquid volume fraction was set to a constant  $\phi_l = 1$  and time derivatives were set to zero.

In this case, the momentum (11) and energy (12) equations reduce to

$$\nabla \mathbf{u} \cdot \mathbf{u} + \nabla p - 2\nabla \cdot \text{sym} \nabla \mathbf{u} + \text{Gr } b \hat{\mathbf{g}} = 0, \quad (17)$$

$$\mathbf{u} \cdot \nabla T - \frac{1}{\text{Pr}} \nabla \cdot (\kappa \nabla T) = 0 \quad (18)$$

These equations were solved with the same mixed finite elements and Newton method as from Section 3. The high Grashof number, Gr, caused the nonlinear solver to diverge. To handle this, the relaxation and continuation algorithm from Figure 1 was applied to Gr instead of  $\sigma$ . For this problem, Newton's method converged optimally when solving in sequence Gr/16, Gr/8, Gr/4, Gr/2, and finally Gr. In the Sapphire code [22], both Gr and  $\sigma$  continuation are handled by the same routine which allows the regularization parameter to be specified. To begin the time dependent simulation, the cold wall was dropped to  $T_c = -1$  while the hot wall remained at  $T_h = 1$ . This caused freezing from right to left. Note that the temperature scaling was unchanged, so the physical temperature of the cold wall was  $\mathcal{T}_c = -10^\circ\text{C}$ , as it was in the experiment.

### 5.2.2. Sensitivity to numerical parameters

For this sensitivity study, the nominal parameter values were  $h = 0.01$ ,  $\Delta t = 0.06$ ,  $\sigma = 0.004$ ,  $\tau = 10^{-12}$ , and  $q = 4$ . From their nominal values, each parameter was varied independently. The resulting phase interfaces were compared at time  $t = 1.6$ . The results are shown in Figure 7. The time  $t = 1.6$  is also the final simulated time presented in Figure 8.

The mesh cell size,  $h$ , was varied from a maximum of  $h = 0.04$  to a minimum of  $h = 0.005$ . The largest size,  $h = 0.04$ , significantly degraded the solution. The solution appeared to converge asymptotically as  $h$  was reduced. Between the smallest two values,  $h = 0.01$  and  $h = 0.005$ , there was almost no change near either the top or bottom wall, and only a minor difference in the center. This result is better than was seen for the octadecane melting simulation in Section 5.1, where there was a much larger sensitivity to  $h$  when using the same values. The time step size,  $\Delta t$ , was varied from a maximum of  $\Delta t = 0.03$  to a minimum of  $\Delta t = 0.012$ . Nearly no sensitivity was observed between these settings. The regularization parameter,  $\sigma$ , was varied from a maximum of  $\sigma = 0.008$  to a minimum of  $\sigma = 0.001$ . The solution appeared to be approaching an asymptotic limit. The difference between the two smallest values,  $\sigma = 0.002$  and  $\sigma = 0.001$ , was barely visible. The solid velocity relaxation parameter  $\tau$  was varied from a maximum of  $\tau = 10^{-6}$  to

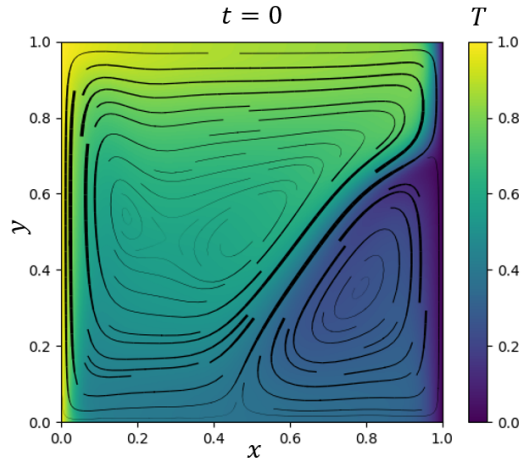


Figure 6: Steady state solution for natural convection of water. The top and bottom walls were adiabatic. The temperature of the right wall was held constant at the freezing point, while the temperature of the left wall was held constant at a higher temperature. The similarity parameters were  $Gr = 3.60 \times 10^5$  and  $Pr = 6.99$ . The numerical parameters were  $h = 0.005$  and  $q = 2$ . The temperature field is shown with a color scale and the velocity streamlines are shown in black. The thickness of the streamlines is linearly proportional to the local velocity magnitude. Two convection cells resulted from the density anomaly of water, where its thermal expansion coefficient changes signs. Between the two cells, the temperature is that of the density anomaly. This steady state solution was used as the initial values for the freezing simulation in Figure 8.

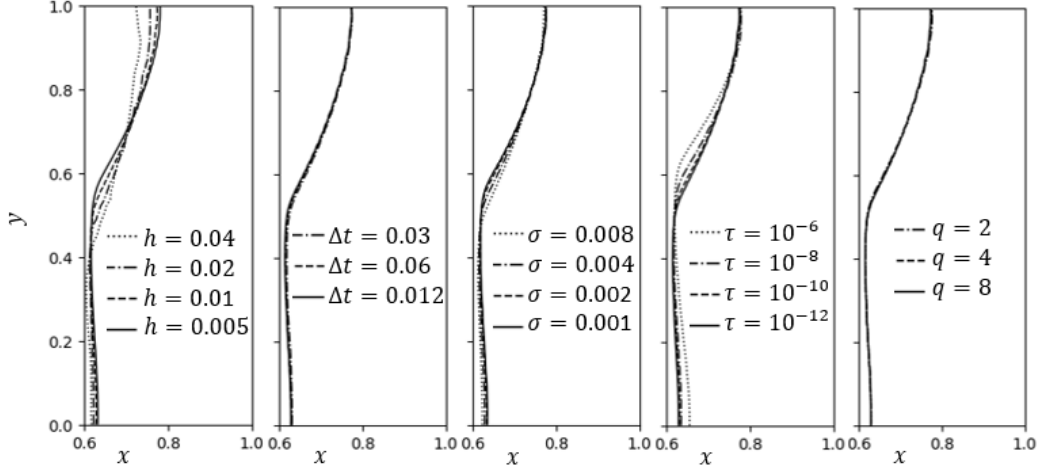


Figure 7: Sensitivity study for the water freezing simulation.

Five numerical parameters were varied. These were the mesh cell size  $h$ , the time step size  $\Delta t$ , the phase interface regularization parameter  $\sigma$ , the solid velocity relaxation parameter  $\tau$ , and the quadrature degree  $q$ . With respect to nominal values, each parameter was varied individually and the resulting phase interfaces were evaluated at time  $t = 1.6$ . The nominal values were  $h = 0.01$ ,  $\Delta t = 0.06$ ,  $\sigma = 0.004$ ,  $\tau = 10^{-12}$  and  $q = 4$ . Asymptotic limits are apparent for all five parameters. Between the smallest two values of  $h$ , i.e.  $h = 0.01$  to  $h = 0.005$ , there is a minor change near the center of the phase interface. Insensitivity is successfully demonstrated for small  $\Delta t$ ,  $\sigma$ , and  $\tau$ , and for large  $q$ .

a minimum of  $\tau = 10^{-12}$ . For the largest value  $\tau = 10^{-6}$ , significantly more freezing occurred near the center and less freezing occurred near the bottom wall. The solution appeared to be approaching an asymptotic limit. Between the two smallest values of  $\tau$ ,  $\tau = 10^{-10}$  and  $\tau = 10^{-12}$ , the change is barely visible. The quadrature degree,  $q$ , was varied between  $q = 2$ ,  $q = 4$ , and  $q = 8$ . This had no significant effect on the solution.

### 5.2.3. Results and discussion

The sensitivity study revealed that large time step sizes  $\Delta t$  can be used without significantly changing the resulting phase interface. To most easily compare to experimental results in [4], solutions were obtained at every one-hundred physical seconds, corresponding to a simulated time step size of about  $\Delta t = 0.0695$ . Figure 8 visualizes results at times  $t = 0$ ,  $t = 0.35$ , and  $t = 1.6$ . As freezing proceeded from right to left, the two circulating regions of natural convection were maintained, translating to the left along with the phase interface. The bottom circulating region showed a lower tem-

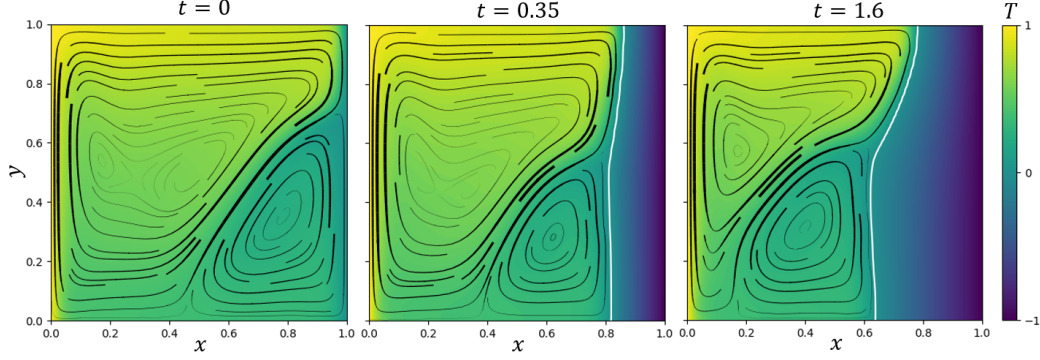


Figure 8: Water freezing simulation results at three times.

The top and bottom walls were adiabatic. Initially, the temperature of the right wall was kept constant at the freezing point. The temperature of the left wall was kept constant at a higher temperature to cause natural convection. Two convection cells resulted from the density anomaly of water. After the natural convection reached a steady state, at  $t = 0$ , the temperature of the right wall was dropped below the freezing point to cause freezing from right to left. Phase-dependent material properties were included with  $\rho_s/\rho_l = 0.917$ ,  $c_{p,s}/c_{p,l} = 0.531$ , and  $k_s/k_l = 3.77$ . The similarity parameters were  $\text{Gr} = 3.60 \times 10^5$ ,  $\text{Pr} = 6.99$ , and  $\text{Ste} = 0.125$ . The numerical parameters were  $h = 0.005$ ,  $\Delta t = 0.0695$ ,  $\sigma = 0.004$ ,  $\tau = 10^{-10}$ , and  $q = 2$ . Left) The initial values, obtained by solving the steady state natural convection problem as explained in Section 5.2.1. The temperature field is shown with a color scale and the velocity streamlines are shown in black. The thickness of the streamlines is linearly proportional to the velocity magnitude. Center) The solution at  $t = 0.35$ , corresponding to 500 seconds. The white line is a isoline where  $T = 0$ , indicating the phase interface. Right) The same at  $t = 1.60$ , corresponding to 2300 seconds.

perature and velocity. The freezing front was nearly planar and proceeded more rapidly in this region. The top circulating region had higher temperature and velocity. The freezing front was curved and proceeded less rapidly near the top wall. Also, near the phase interface, note the sharper temperature gradient near the top wall. This slowed the freezing process in that region.

At  $t = 1.6$ , after a total of twenty-three time steps, 1812 Newton iterations were used in total. This averages to about eighty Newton iterations per time step. This includes all iterations from intermediate problems during the continuation procedure sketched in Figure 1. For all time steps, the largest intermediate regularization parameter value was  $\sigma = 4.096$ . For the first time step, four intermediate values of  $(\sigma = 2.05, 1.027, 0.5155, 0.25975)$  were needed between  $\sigma = 4.096$  and the targeted value,  $\sigma = 0.004$ . At  $t = 1.6$ , an additional four values of  $(\sigma = 0.131875, 0.09990625, 0.0679375, 0.03596875)$

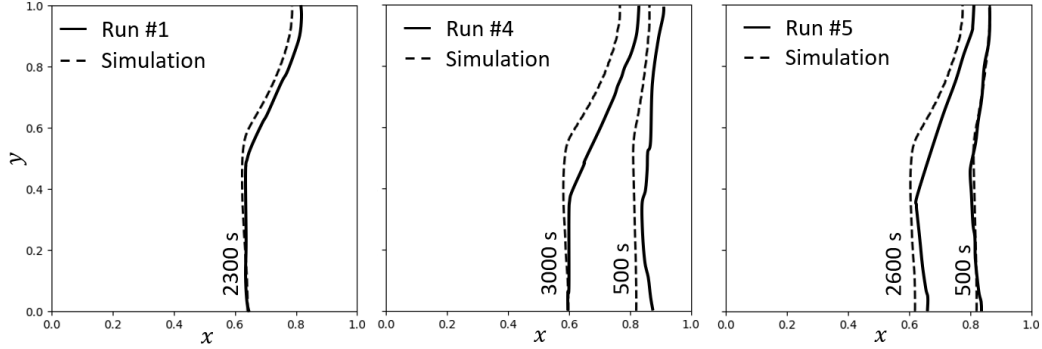


Figure 9: Freezing simulation results compared to multiple experimental runs from [4]. The same simulation results are compared to the three experimental runs. The runs had varied controls on the initial state. Run #1 used “cold start” initial conditions described in [4]. Runs #4 and #5 used “warm start” initial conditions briefly described in Section 5.2.3 and detailed in [4]. The runs also has varied controls for thermal regulation of the test section walls. Runs #1 and #4 had a constant air flow outside the walls of the test section. For run #5, the test section was instead submerged in a water bath. For the simulation, the initial values were based on the “warm start” procedure, as described in Section described in Section 5.2.3. Also, for the simulation, the top and bottom walls were assumed to be adiabatic.

were needed.

Figure 9 compares the simulation results to a group of experimental runs from [4]. The simulation compares remarkably well to experimental run #1; but that run reportedly used a “cold start”. The simulation used a “warm start”, which corresponds to the experimental runs #4 and #5. It was also shown in [4] that the freezing process was sensitive to the thermal control of the test section walls. Experimental runs #1 and #4 had a constant air flow around the walls. For run #5, the test section was submerged in a water bath. The importance of simulating three-dimensional heat transfer in the side walls was further demonstrated in [10]. There, it was also noted that the viscosity of water substantially increases near its freezing temperature, and that this in return substantially affects the freezing process. Further investigating the effects of a temperature dependent viscosity or heat transfer through the test section walls was outside the scope of this work.

## 6. Conclusions

An enthalpy method was used to simulate convection-coupled isothermal phase-change on a single geometric domain. The governing equations were

discretized in space with mixed finite elements and in time with backward difference formulas. The resulting system of nonlinear equations was solved with Newton’s method. As new contributions, the current work

- applied a general regularization approach to the isothermal phase-change equation of state, which yields a function for the liquid volume fraction which is qualitatively similar to that from [13, 14].
- simplified the stabilization of the mixed finite element formulation. In [13, 14], both Taylor-Hood elements and the pressure penalty method were used in combination. In the current work, equal order elements were stabilized with the pressure penalty method alone.
- designed an efficient continuation procedure capable of robustly solving the nonlinear problem for a variety of physical and numerical parameters. Without this procedure, previous literature [13, 14] relied on adaptive mesh refinement, carefully selected time step sizes, specifying a one-way melting or solidification process, and initializing the new phase in part of the domain.
- verified the solver’s accuracy to second order in space and time via a convergence study, using the method of manufactured solutions.
- presented simulations for the melting of octadecane and one for the freezing of water. For each, a sensitivity study was performed with respect to five numerical parameters. These were the mesh cell size  $h$ , the time step size  $\Delta t$ , the phase interface regularization parameter  $\sigma$ , the solid velocity relaxation parameter  $\tau$ , and the quadrature degree  $q$ . In both cases, it was demonstrated that the results could be obtained which were not sensitive to  $\Delta t$ ,  $\sigma$ ,  $\tau$ , or  $q$ . For the water freezing case, sensitivity to  $h$  was also minor between the two smallest values. For the octadecane melting case, results were still visibly sensitive to  $h$ , though an asymptotic convergence behavior was observed. Further reducing  $h$  was impractical, because it would increase the number of degrees of freedom in the linear system quadratically. This would be especially computationally intensive for the employed direct linear system solver.
- compared results from the two simulation cases to experimental data sets from the literature, namely [3] for melting octadecane and [4] for freezing water. For the case of melting octadecane, the simulated phase interface shows good agreement to the experiment in the interior, while



there were large discrepancies near the adiabatic walls. The water freezing simulation was compared to multiple experimental runs. The runs use varied procedures for controlling initial conditions and thermal regulation of the test section walls. While the simulated phase interface compared well to one of the runs, that run reportedly used a different procedure for initialization which is not considered by the simulation. More information is needed to accurately define the initial conditions for the water freezing case, and adiabatic wall assumptions are too ideal for both cases.

- shared the open source code in a new Python packaged called Sapphire [22], using the finite element library Firedrake [21]. Sapphire’s test suite covers many of the results of this paper. Reproducing exact results is only a matter of setting the described parameter values. The versions of Sapphire and Firedrake were documented with DOI’s on Zenodo, respectively at [22] and [29].

The implementation in Sapphire [22] is flexible, and can readily be applied to problems with other geometries, parameters, initial values, and boundary conditions. By using UFL [23] for defining the mathematical model symbolically, the model is easily modifiable and extensible. As a next step, we want to apply the approach to non-isothermal phase-change involving mushy layers, e.g. melting and refreezing cycles of salt water. The continuation procedure has been robust for convection-coupled isothermal phase-change, and there is reason to believe that it will also work well, if not better, for the case of non-isothermal phase-change. Still, there may exist a more general approach to regularizing such nonlinear problems, and this is also worth exploring. There are also promising routes for reducing computational costs. One route would be the application of iterative linear system solvers, which would require the development of a preconditioner. Such an iterative solver would make three-dimensional geometries tractable, and would also open opportunities for addressing inverse problems.

## Acknowledgments

The authors were funded in part by the Excellence Initiative of the German Federal and State Governments through grant GSC 111. The work was furthermore supported by the Federal Ministry of Economic Affairs and Energy, on the basis of a decision by the German Bundestag (50 NA 1502).

## References

## References

- [1] E. Sparrow, R. R. Schmidt, J. W. Ramsey, Experiments on the role of natural convection in the melting of solids, *Journal of Heat Transfer* 100 (1978).
- [2] E. Sparrow, J. W. Ramsey, R. G. Kemink, Freezing controlled by natural convection, *Journal of Heat Transfer* 101 (1979).
- [3] M. Okada, Analysis of heat transfer during melting from a vertical wall, *International Journal of Heat and Mass Transfer* 27 (1984) 2057–2066.
- [4] T. A. Kowalewski, M. Rebow, Freezing of water in a differentially heated cubic cavity, *International Journal of Computational Fluid Dynamics* 11 (1999) 193–210.
- [5] K. Schüller, B. Berkels, J. Kowalski, Integrated modeling and validation for phase change with natural convection, in: M. Schäfer, M. Behr, M. Mehl, B. Wohlmuth (Eds.), *Recent Advances in Computational Engineering*, volume 124 of *Lectures Notes in Computational Science and Engineering (LNCSE)*, Springer, 2017, pp. 127–144.
- [6] V. Voller, M. Cross, N. Markatos, An enthalpy method for convection/diffusion phase change, *International Journal for Numerical Methods in Engineering* 24 (1987) 271–284.
- [7] V. Alexiades, A. Solomon, *Mathematical modeling of melting and freezing processes*, Bristol, PA (United States); Hemisphere Publishing, 1992.
- [8] V. R. Voller, C. Prakash, A fixed grid numerical modelling methodology for convection-diffusion mushy region phase-change problems, *International Journal of Heat and Mass Transfer* 30 (1987) 1709–1719.
- [9] A. Brent, V. Voller, K. Reid, Enthalpy-porosity technique for modeling convection-diffusion phase change: application to the melting of a pure metal, *Numerical Heat Transfer, Part A: Applications* 13 (1988) 297–318.

- [10] M. Giangi, T. A. Kowalewski, F. Stella, E. Leonardi, Natural convection during ice formation: numerical simulation vs. experimental results, *Computer Assisted Mechanics and Engineering Sciences* 7 (2000) 321–342.
- [11] K. J. Evans, D. A. Knoll, Temporal accuracy analysis of phase change convection simulations using the JFNK-SIMPLE algorithm, *International Journal for Numerical Methods in Fluids* 55 (2007) 637–653.
- [12] Y. Belhamadia, A. S. Kane, A. Fortin, An enhanced mathematical model for phase change problems with natural convection, *International Journal of Numerical Analysis and Modeling* 3 (2012) 192–206.
- [13] I. Danaila, R. Moglan, F. Hecht, S. Le Masson, A Newton method with adaptive finite elements for solving phase-change problems with natural convection, *Journal of Computational Physics* 274 (2014) 826–840.
- [14] A. G. Zimmerman, J. Kowalski, Monolithic simulation of convection-coupled phase-change: Verification and reproducibility, in: M. Schäfer, M. Behr, M. Mehl, B. Wohlmuth (Eds.), *Recent Advances in Computational Engineering*, volume 124 of *Lectures Notes in Computational Science and Engineering (LNCSE)*, Springer, 2017, pp. 177–197.
- [15] A. Rakotondrandisa, I. Danaila, L. Danaila, Numerical modelling of a melting-solidification cycle of a phase-change material with complete or partial melting, *International Journal of Heat and Fluid Flow* 76 (2019) 57–71.
- [16] S. Wang, A. Faghri, T. L. Bergman, A comprehensive numerical model for melting with natural convection, *International Journal of Heat and Mass Transfer* 53 (2010) 1986–2000.
- [17] V. Voller, C. Swaminathan, B. G. Thomas, Fixed grid techniques for phase change problems: a review, *International Journal for Numerical Methods in Engineering* 30 (1990) 875–898.
- [18] J. Woodfield, M. Alvarez, B. Gómez-Vargas, R. Ruiz-Baier, Stability and finite element approximation of phase change models for natural convection in porous media, *Journal of Computational and Applied Mathematics* 360 (2019) 117–137.

- [19] J. Donea, A. Huerta, Finite element methods for flow problems, John Wiley & Sons, 2003.
- [20] U. M. Ascher, L. R. Petzold, Computer methods for ordinary differential equations and differential-algebraic equations, volume 61, SIAM, 1998.
- [21] F. Rathgeber, D. A. Ham, L. Mitchell, M. Lange, F. Luporini, A. T. T. McRae, G.-T. Bercea, G. R. Markall, P. H. J. Kelly, Firedrake: automating the finite element method by composing abstractions, *ACM Transactions on Mathematical Software* 43 (2016) 24:1–24:27.
- [22] A. G. Zimmerman, geo-fluid-dynamics/sapphire: Convection-coupled phase-change verification and preliminary validation, <https://doi.org/10.5281/zenodo.3250317>, 2019.
- [23] M. S. Alnæs, A. Logg, K. B. Ølgaard, M. E. Rognes, G. N. Wells, Unified form language: A domain-specific language for weak formulations of partial differential equations, *ACM Transactions on Mathematical Software* 40 (2012) 9.
- [24] S. Balay, S. Abhyankar, M. F. Adams, J. Brown, P. Brune, K. Buschelman, L. Dalcin, V. Eijkhout, W. D. Gropp, D. Kaushik, M. G. Knepley, D. A. May, L. C. McInnes, R. T. Mills, T. Munson, K. Rupp, P. Sanan, B. F. Smith, S. Zampini, H. Zhang, PETSc Users Manual, Technical Report ANL-95/11 - Revision 3.9, Argonne National Laboratory, 2018.
- [25] S. Balay, W. D. Gropp, L. C. McInnes, B. F. Smith, Efficient management of parallelism in object oriented numerical software libraries, in: E. Arge, A. M. Bruaset, H. P. Langtangen (Eds.), *Modern Software Tools in Scientific Computing*, Birkhäuser Press, 1997, pp. 163–202.
- [26] L. D. Dalcin, R. R. Paz, P. A. Kler, A. Cosimo, Parallel distributed computing using Python, *Advances in Water Resources* 34 (2011) 1124–1139. *New Computational Methods and Software Tools*.
- [27] P. Amestoy, I. Duff, J. L’Excellent, J. Koster, A fully asynchronous multifrontal solver using distributed dynamic scheduling, *SIAM Journal on Matrix Analysis and Applications* 23 (2001) 15–41.

- [28] P. Amestoy, A. Guermouche, J. L'Excellent, S. Pralet, Hybrid scheduling for the parallel solution of linear systems, *Parallel Computing* 32 (2006) 136–156.
- [29] zenodo/Firedrake-20190620.0, Software used in 'Simulating convection-coupled phase-change in enthalpy form with mixed finite elements', <https://doi.org/10.5281/zenodo.3250636>, 2019.
- [30] P. J. Roache, Code verification by the method of manufactured solutions, *Journal of Fluids Engineering* 124 (2002) 4–10.
- [31] T. Michałek, T. A. Kowalewski, Simulations of the water freezing process—numerical benchmarks, *Task Quarterly* 7 (2003) 389–408.
- [32] B. Gebhart, J. C. Mollendorf, A new density relation for pure and saline water, *Deep Sea Research* 24 (1977) 831–848.